7-1-2017

Modeling Micro-Porous Surfaces for Secondary Electron Emission Control to Suppress Multipactor

J. M. Sattler
Air Force Institute of Technology

Ronald A. Coutu Jr.
Marquette University, ronald.coutu@marquette.edu

R. Lake
Air Force Institute of Technology

T. Laurvick
Air Force Institute of Technology

T. Back
Air Force Research Laboratory

See next page for additional authors

Accepted version. Journal of Applied Physics, Vol. 122, No. 5 (July 2017): 055304. DOI.

Modeling Micro-Porous Surfaces for Secondary Electron Emission Control to Suppress Multipactor

J. M. Sattler
Department of Electrical and Computer Engineering, Air Force Institute of Technology, Wright-Patterson Air Force Base, OH
R. A. Coutu Jr.
Department of Electrical and Computer Engineering, Marquette University, Milwaukee, WI
R. Lake
Department of Electrical and Computer Engineering, Air Force Institute of Technology, Wright-Patterson Air Force Base, OH
T. Laurvick
Department of Electrical and Computer Engineering, Air Force Institute of Technology, Wright-Patterson Air Force Base, OH

T. Back
Materials and Manufacturing Directorate, Air Force Research Laboratory, Wright-Patterson Air Force Base, OH
S. Fairchild
Materials and Manufacturing Directorate, Air Force Research Laboratory, Wright-Patterson Air Force Base, OH

Abstract

This work seeks to understand how the topography of a surface can be engineered to control secondary electron emission (SEE) for multipactor suppression. Two unique, semi-empirical models for the secondary electron yield (SEY) of a micro-porous surface are derived and compared. The first model is based on a two-dimensional (2D) pore geometry. The second model is based on a three-dimensional (3D) pore geometry. The SEY of both models is shown to depend on two categories of surface parameters: chemistry and topography. An important parameter in these models is the probability of electron emissions to escape the surface pores. This probability is shown by both models to depend exclusively on the aspect ratio of the pore (the ratio of the pore height to the pore diameter). The increased accuracy of the 3D model (compared to the 2D model) results in lower electron escape probabilities with the greatest reductions occurring for aspect ratios less than two. In order to validate these models, a variety of micro-porous gold surfaces were designed and fabricated using photolithography and electroplating processes. The use of an additive metal-deposition process (instead of the more commonly used subtractive metal-etch process) provided geometrically ideal pores which were necessary to accurately assess the 2D and 3D models. Comparison of the experimentally measured SEY data with model predictions from both the 2D and 3D models illustrates the improved accuracy of the 3D model. For a micro-porous gold surface consisting of pores with aspect ratios of two and a 50% pore density, the 3D model predicts that the maximum total SEY will be one. This provides optimal engineered surface design objectives to pursue for multipactor suppression using gold surfaces.

I. INTRODUCTION

For over seventy years, surface topography has been understood to influence the yield of secondary electron emissions (SEE) from a given material.[1–6] During the 1930s and 1940s, advances in vacuum electron devices drove interest towards SEE research.[1–3] This research demonstrated the first use of artificially roughened or porous surfaces to reduce the secondary electron yield (SEY) of metals.[1–4] However, these SEY reductions were difficult to precisely control due to the limited surface engineering techniques of the time. Examples of these techniques include using a flame of burning turpentine to deposit a layer of carbon soot, directly spraying a suspension of carbon soot, or depositing various metals using metal sublimation or evaporation.[1,2,4] Subsequent interest in controlling SEE diminished until the 1960s when new technologies involving high-power microwave devices, particle accelerators, and space-based systems began encountering problems with a SEE resonance phenomenon called multipactor. Multipactor can be described as an avalanche of electrons caused by recurring SEE in resonance with a time-varying electric field. For multipactor to occur, the material(s) involved must have a SEY > 1 over the energy range of the emitted electrons (typically several hundred eV). Consequently, an engineered surface with a SEY ≤ 1 will suppress any multipactor.

Despite this knowledge, the vast majority of multipactor suppression research has focused on other methods including geometrical modifications, elimination of cavities, low-SEY coatings, RF conditioning, DC electrode biasing, applied magnetic fields, and power restrictions.[7–25] More recently, low-SEY coatings and other surface treatments have seen an increase in research interest.[26–35] Only in the last five years has there been a revitalization of research into using engineered surfaces to control SEE for multipactor suppression.[36–42] The results from these efforts show tremendous promise for new multipactor suppression solutions, in part because they take advantage of modern surface engineering tools and techniques that provide the ability to precisely tailor surface topographies at micro- and nanoscales.

In this paper, we explore micro-porous surfaces to better understand the most effective methods to control SEE by engineering the topography of a surface. To do this, we derive 2D and 3D semi-empirical total SEY models for porous surfaces and compare them to SEY measurements made on micro-porous gold surfaces. Because multipactor involves large numbers of secondary electrons (on the order of 10^4–10^{10} cm^{-3}), it is appropriate to use statistical probabilities of electron emissions to model the SEY of a porous surface.[43–45] Both models are based on perfectly symmetrical pore geometries and depend on four variables: two empirically measured SEY values (one for the surfaces at the bottoms of pores and one for the surfaces in-between pores), the pore aspect ratio (ratio of the pore height to the pore diameter), and the pore density (commonly known as porosity). We use a gold electroplating process to fabricate the micro-porous gold surfaces for SEY measurements. This surface engineering technique yields pores that closely resemble the symmetrical pore geometry used to develop the SEY models, providing increased equivalence between model predictions and experimental results. The experimental results agree reasonably well with SEY predictions from the models and confirm that the 3D model is more accurate than the 2D model.

II. ANALYTICAL SEY MODELING FOR POROUS SURFACES

Determining optimal surface topographies to control SEE for multipactor suppression requires an accurate model to predict the SEY of an engineered surface. Figure 1(a) shows the geometry of a porous surface with total SEY parameters σ_{pore} and $\sigma_{non\text{-}pore}$, which account for both true secondary and backscattered electrons. Ye *et al.*[38] showed that a weighted average of the parameters σ_{pore} and $\sigma_{non\text{-}pore}$ (with surface porosity providing the weight) can be used to determine an effective SEY of the porous surface which is given as

$$\sigma_{porous-surface} = \sigma_{pore}(\text{Porosity}) + \sigma_{non-pore}(1 - \text{Porosity}), \quad (1)$$

where *Porosity* is the ratio of the pore surface area to the total surface area. The parameter $\sigma_{non\text{-}pore}$ can be determined experimentally through SEY measurements of an unpatterned region of the non-pore surface. Regarding the parameter σ_{pore}, we must consider that the SEY of the surfaces at the bottoms of the pores ($\sigma_{pore\text{-}bottom}$) may not be equivalent to the SEY in the non-pore regions ($\sigma_{non\text{-}pore}$), as shown by the speckled surface regions in Fig. 1(b). This is because any surface engineering technique

used to fabricate the pores (chemical etching, laser ablation, electroplating, etc.) will likely result in chemical and topographical variations between the two surfaces. Thus, the parameter σ_{pore} becomes

$$\sigma_{\text{pore}} = \sigma_{\text{pore-bottom}}\left(P_{\text{escape}}\right), \quad (2)$$

where P_{escape} is the probability of an electron emitted from the bottom surface of a pore, to escape the pore and contribute to $\sigma_{\text{porous-surface}}$. The parameter $\sigma_{\text{pore-bottom}}$ can be determined experimentally through SEY measurements of an unpatterned region of the pore-bottom surface. The parameter P_{escape} can be determined for both 2D and 3D pore models under the following assumptions: electron emissions follow linear trajectories; electrons that impact the pore sidewall are recaptured (i.e., we only consider 1st generation SEE); the location of electron emission from the bottom of a pore is random and uniformly distributed, the azimuthal angle of electron emissions is a uniformly distributed random variable, the polar angle of electron emissions is a cosine-distributed[46] random variable, and all three of these random variables are independent.

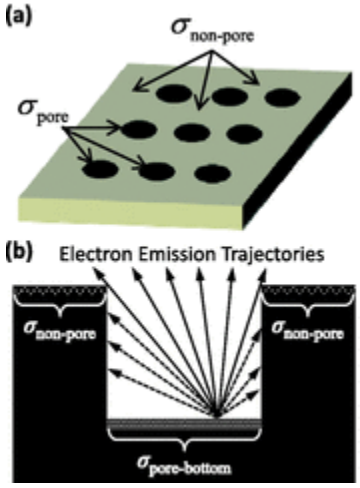

FIG. 1. Porous surface geometry used to develop 2D and 3D secondary electron yield (SEY) models: (a) 3D layout showing distinct SEY parameters for the pore and non-pore surface regions; and (b) 2D cross section of a single pore showing distinct SEY parameters for the pore-bottom and non-pore regions.

A. Two-dimensional SEY model

Figure 2 illustrates the layout of the 2D pore model as well as the parameters used to derive P_{escape} for the 2D case, which we label $P_{\text{escape-2D}}$. This layout is similar to the layout used by Ye *et al.*[38] to derive a formula for the SEY of a 2D rectangular well, with minor modifications to variables and a distinction between the unique surfaces at the bottom and top of the pore. From the geometry shown in Fig. 2, the maximum polar emission angles that permit electron emission are given by

$$\theta_1 = \arctan\left(\frac{R+r}{H}\right) \quad \text{and} \quad \theta_2 = \arctan\left(\frac{R-r}{H}\right), \quad (3)$$

where R is the pore radius, H is the pore height, and r is the distance from the pore center to the emission site. Applying the cosine distribution for the SEE polar angle and summing over the polar

emission angles that permit electron escape provide two probabilities which are conditionally based on the azimuthal emission direction, denoted by φ

$$P_{\text{escape}-2\text{D}} = \begin{cases} \int_0^{\theta_1} \cos(\theta)\, d\theta = \sin(\theta_1), & \text{for } \phi = \pi \\ \int_0^{\theta_2} \cos(\theta)\, d\theta = \sin(\theta_2), & \text{for } \phi = 0. \end{cases} \quad (4)$$

The two conditional probabilities in Eq. (4) can be averaged according to their probability of occurrence (i.e., the probability that φ = π and φ = 0) to yield a mean probability of escape. This is done by noting that the azimuthal emission angle, φ, is a uniformly distributed discrete random variable (for the 2D pore model, φ can only be π or 0). A uniformly distributed discrete random variable with only two outcomes must have equi-probable outcomes equal to one-half. Thus, Eq. (4) is rewritten as a mean probability

$$\bar{P}_{\text{escape}-2\text{D}} = \frac{1}{2}\sin\left[\arctan\left(\frac{R+r}{H}\right)\right] + \frac{1}{2}\sin\left[\arctan\left(\frac{R-r}{H}\right)\right]. \quad (5)$$

We now examine the variable *r* that describes the emission location which was previously assumed to be random and uniformly distributed. For the 2D pore model, *r* maps directly to the emission location and thus can be described as a uniformly distributed random variable with a probability density function, $f_r = 1/R$. In order to simplify Eq. (5) to provide a single-valued probability for a specific pore height and radius, we are interested in determining a value of *r* for which the probability of emissions for all *r* below this value equals the probability of emissions for all *r* above this value. This point represents the statistical median of *r*, denoted r_{med}, and can be determined by solving the following equation for r_{med}:

$$\int_0^{r_{\text{med}}} f_r\, dr = \int_{r_{\text{med}}}^{R} f_r\, dr. \quad (6)$$

For the 2D geometry, solving Eq. (6) provides $r_{\text{med}} = R/2$. Substituting this value of *r* into Eq. (5) and converting the pore height and radius into an aspect ratio ($A_R = H/2R$) provide

$$\bar{P}_{\text{escape}-2\text{D}} = \frac{1}{2}\sin\left[\arctan\left(\frac{3}{4A_R}\right)\right] + \frac{1}{2}\sin\left[\arctan\left(\frac{1}{4A_R}\right)\right]. \quad (7)$$

Combining Eq. (7) with Eq. (1) and Eq. (2) yields the final SEY model for a micro-porous surface based on a 2D pore geometry.

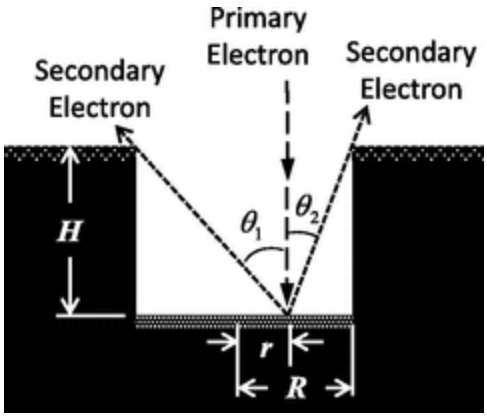

FIG. 2. Illustration of the 2D pore model showing key parameters.[38]

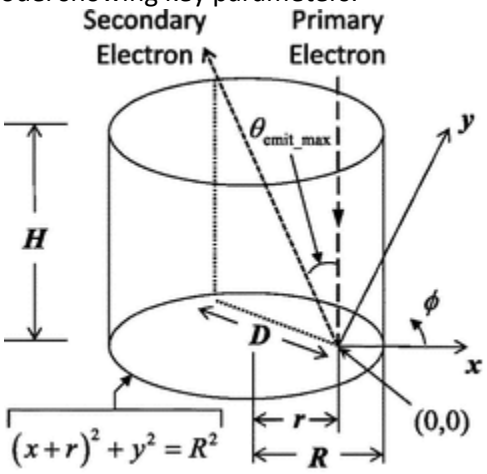

FIG. 3. Illustration of the 3D pore model showing key parameters.

B. Three-dimensional SEY model

Figure 3 illustrates the layout of the 3D pore model as well as the parameters used to derive P_{escape} for the 3D case which we label $P_{escape\text{-}3D}$. Finding an expression for the maximum polar emission angle, ϑ_{emit_max}, requires an expression for the distance, D (as shown in Fig. 3), between the emission location and the circle in the x–y plane that describes the pore sidewall. This circle is given by the equation

$$(x + r)^2 + y^2 = R^2 \text{..} \quad (8)$$

Substituting $x = D\cos(\varphi)$ and $y = D\sin(\varphi)$ into Eq. (8) and rearranging terms yield the quadratic equation

$$D^2 + (2r\cos\phi)D + (r^2 - R^2) = 0. \quad (9)$$

Solving Eq. (9) for D provides

$$D = \sqrt{R^2 - r^2\sin^2\phi} - r\cos\phi. \quad (10)$$

Thus, the maximum polar emission angle, ϑ_{emit_max}, is given by

$$\theta_{\text{emit\_max}} = \arctan\left(\frac{D}{H}\right) = \arctan\left(\frac{\sqrt{R^2 - r^2\sin^2\phi} - r\cos\phi}{H}\right). \quad (11)$$

Applying the cosine distribution for the SEE polar angle and summing over the polar emission angles that permit electron escape provide

$$P_{\text{escape}-3\text{D}} = \int_0^{\theta_{\text{emit}_{\text{max}}}} \cos(\theta)\, d\theta = \sin\left(\theta_{\text{emit}_{\text{max}}}\right) = \sin\left[\arctan\left(\frac{\sqrt{R^2 - r^2\sin^2\phi} - r\cos\phi}{H}\right)\right]. \quad (12)$$

For the 2D model, the azimuthal emission angle, ϕ, was a discrete (binary) random variable; however, for the 3D model, ϕ is a continuous random variable over the range of $0 \le \phi < 2\pi$. Thus, the mean probability of escape over the infinite number of conditional probabilities in the range of $0 \le \phi < 2\pi$ is

$$\bar{P}_{\text{escape}-3\text{D}} = \frac{1}{2\pi}\int_0^{2\pi} \sin\left[\arctan\left(\frac{\sqrt{R^2 - r^2\sin^2\phi} - r\cos\phi}{H}\right)\right]\, d\phi. \quad (13)$$

For the 2D case, r mapped directly to the emission location and thus was uniformly distributed from 0 to R, and for the 3D case, r no longer maps uniformly to the random (uniformly distributed) emission location. This is logical when considering the fact that it is more probable for emissions to occur at larger values of r because the circle of possible emission locations increases as the radius increases. For the 3D model, r is now distributed according to

$$f_r = \frac{2\pi r}{\pi R^2} = \frac{2r}{R^2}. \quad (14)$$

Substituting Eq. (14) into Eq. (6) and solving for r_{med} provide $r_{\text{med}} = R/\sqrt{2}$. Substituting this median value of r into (13) and converting to an aspect ratio ($A_R = H/2R$) provide

$$\bar{P}_{\text{escape}-3\text{D}} = \frac{1}{2\pi}\int_0^{2\pi} \sin\left[\arctan\left(\frac{\sqrt{1+\cos^2\phi} - \cos\phi}{2A_R\sqrt{2}}\right)\right]\, d\phi. \quad (15)$$

Although the integral in Eq. (15) cannot be solved in closed form, we can evaluate it numerically. Combining Eq. (15) with Eq. (1) and Eq. (2) provides the final SEY model for a micro-porous surface based on a 3D pore geometry.

C. Analysis of models

Both the 2D and 3D models are functions of four variables: $\sigma_{\text{pore-bottom}}$, $\sigma_{\text{non-pore}}$, *Porosity*, and A_R. The first two variables are intrinsically linked to the material chemistry and thus will be influenced by both the type of bulk material and the changes in surface chemistry with exposure to the atmosphere. It should be noted that these variables ($\sigma_{\text{pore-bottom}}$ and $\sigma_{\text{non-pore}}$) can represent single values of SEY coefficients (such as the maximum SEY) or they can represent a portion of the energy-dependent SEY curve. By contrast, the second two variables are only functions of the surface topography and thus provide the parameters we seek to leverage, in order to control the SEY of the surface. Figure 4 shows a comparison of the total SEY of an engineered surface for both the 2D and 3D models and using parameters $\sigma_{\text{non-pore}} = 1.7$ and $\sigma_{\text{pore-bottom}} = 1.6$. These values were selected because they are in the range of measured maximum total SEY values for gold provided in an SEY measurement database compiled and published by Joy.[47] The value for $\sigma_{\text{non-pore}}$ was chosen to be slightly higher than that for $\sigma_{\text{pore-bottom}}$ because most surface engineering fabrication processes will provide lower SEY surfaces at the bottoms of the pores. Figure 4 clearly indicates that the 3D model predicts a lower total SEY than the 2D model over all values of *Porosity* and A_R. This difference is caused by the inaccuracies of the simplified 2D model which are accumulated in Eq. (7). Figure 5 further illustrates the model differences by plotting Eqs. (7) and (15) along with a plot of the absolute difference between the two formulae. This absolute difference between the 2D and 3D mean-P_{escape} models peaks at 0.068 ($A_R = 0.44$) and stays above 0.05 over the range of $0.18 < A_R < 1.17$. This is important because the aspect ratio is a critical trade-space parameter in any multipactor suppression design involving engineered surfaces. Although higher aspect ratios are helpful to decrease the probability that electrons will escape, which in turn reduces SEY, they also negatively impact the performance characteristics (e.g., insertion loss) of the RF device in which the engineered surface is incorporated. Therefore, it is vital that any SEY model for an engineered surface be accurate over the range of $0 < A_R < 1$. Consequently, the 3D pore model specified by Eqs. (1), (2), and (15) becomes favored over the 2D model for predicting optimal engineered surface topographies for SEY control. However, the 2D model's closed-form solution remains preferred for low-porosity surfaces (i.e., *Porosity* < 0.15) because the inaccuracies of Eq. (7) are minimized by the weighting function in Eq. (1). This explains why in Fig. 4 the low-porosity curves overlap more than the high-porosity curves.

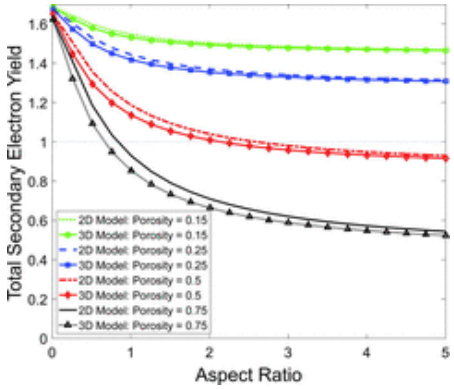

FIG. 4. Analytical modelling results showing the total secondary electron yield for 2D and 3D pore models based on an engineered surface with $\sigma_{\text{non-pore}} = 1.7$ and $\sigma_{\text{pore-bottom}} = 1.6$.

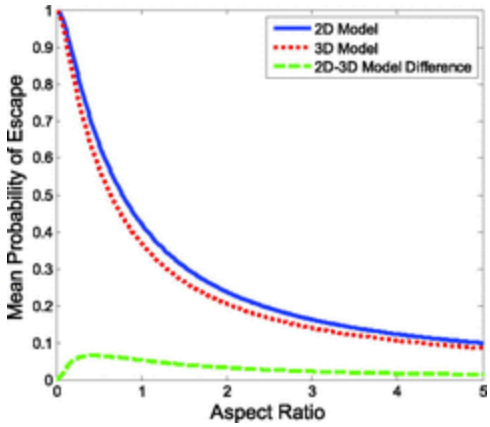

FIG. 5. Comparison of the analytically modelled mean probability of electron escape for 2D and 3D pore models.

III. EXPERIMENTAL METHOD AND RESULTS

A. Micro-porous surface design and fabrication

Micro-porous gold surfaces were fabricated, characterized, and measured to determine their total SEY in order to validate the previously discussed 2D and 3D SEY models. Five microporous patterns were designed with porosities of 0.13, 0.5, and 0.91 and aspect ratios of 0.15 and 0.375. Pore diameters were designed to be 16 μm or 40 μm. The designs were based on a 6 μm gold electroplating process. Gold was chosen for this study because of its low SEY and previously demonstrated success in anti-multipactor coatings.[39] In order to achieve a porosity of 0.91, two of the five patterns were designed with the pores in a closed-packed array.[48] Figure 6 shows the patterns of the five designs as well as the process used to fabricate the micro-porous surfaces. Sample fabrication was carried out in ISO 6 cleanrooms (i.e., Class 1000) at both the Air Force Institute of Technology and the Air Force Research Laboratory. Following fabrication, the samples were characterized using a profilometer and a scanning electron microscope (SEM). The average pore height was measured to be 5.6 μm. Table I provides a summary of the fabrication results. The reductions in the pore diameter (see columns 2 and 3 in Table I) were caused by minor eroding of the photoresist mold that occurred during an oxygen plasma clean of the surfaces prior to electroplating. These reductions in the pore diameter are responsible for the associated changes in porosity and aspect ratio, as also shown in Table I. Figure 7 shows SEM images of samples 1–2 and 3–2, illustrating the excellent micro-porous pattern consistency and uniformity achieved in this effort. The primary fabrication challenge was preventing pore deformation and sidewall discontinuities in the close-packed pore designs (Samples 1–1 and 1–2) as shown by the SEM image inset in Fig. 7(a). Clearly visible in Fig. 7(b) are the near-perfect pore sidewalls that provide the geometry necessary to compare SEY measurements to SEY predictions from the 2D and 3D models. Also evident in Fig. 7(b) are the distinctly different topographies of the pore bottoms (sputtered gold) and non-pore regions (electroplated gold) which support the need to maintain two distinct surface SEY parameters ($\sigma_{\text{non-pore}}$ and $\sigma_{\text{pore-bottom}}$) in the analytical models (Note: the SEY of the electroplated gold will also differ from the sputtered gold due to the different surface chemistries that result from the different fabrication processes).

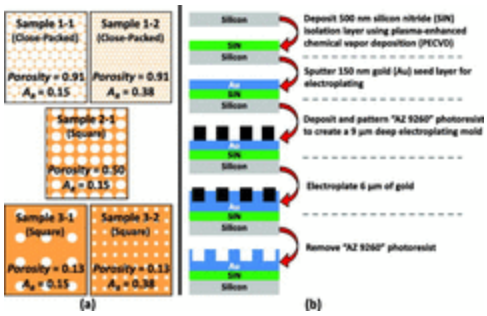

FIG. 6. Micro-porous surfaces used for total SEY measurements: (a) sample designs; and (b) fabrication process.[48]

TABLE I. Micro-porous gold surface fabrication results.

Sample	Designed pore diameter (μm)	Fabricated pore diameter (μm)	Designed porosity	Fabricated porosity	Designed aspect ratio	Fabricated aspect ratio
1-1	40	37.2	0.91	0.75	0.15	0.15
1-2	16	11.5	0.91	0.44	0.38	0.49
2-1	40	34.8	0.50	0.36	0.15	0.16
3-1	40	33.5	0.13	0.09	0.15	0.17
3-2	16	10.4	0.13	0.05	0.38	0.54

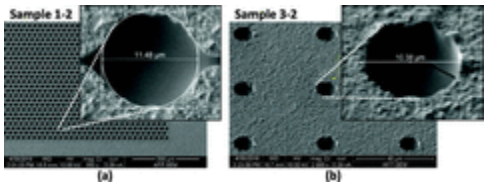

FIG. 7. Scanning Electron Microscopy (SEM) images of micro-porous surfaces previously fabricated and used for model validation:[48] (a) SEM images taken at normal incidence to sample 1-2 showing non-continuous pore sidewalls; and (b) SEM images taken at a 45° incident angle to sample 3-2 showing ideal smooth and vertical pore sidewalls.

B. SEY measurements

SEY measurements were performed in a UHV vacuum chamber at pressures between 1×10^{-9} and 5×10^{-9} Torr. Primary electrons with energy ranging from 50 to 2000 eV were generated by using a STAIB Instruments model DESA-150 analyzer with an integrated 0–5 keV electron gun (e-gun).[49] Electron beam currents were limited to 20 nA to minimize electron conditioning.[36,40] The working distance between the e-gun and the sample was 50 mm. The e-gun orientation follows a north-south path to minimize electron deflection caused by the earth's magnetic field. For this experimental setup, the maximum electron deflection resulting from the earth's magnetic field is 2.5 mm for 50 eV which is small enough to be accounted for by the size of our samples which were 15×15 mm^2 with a porous

region 5.2 × 5.2 mm^2. To ensure that the e-beam illuminated only the porous surfaces, the DESA-150 analyzer was used to briefly image the sample with 1 keV electrons prior to SEY testing. This ensured that the e-beam was centered on the sample so that only the porous region was illuminated. All samples were exposed to atmospheric conditions for at least 48 hours prior to vacuum chamber loading and pump-down. To ensure that the SEY measurements were recorded under typical conditions, no vacuum chamber sample cleaning (e.g., ion sputter cleaning) was performed. A Keithley 6517 A electrometer was used to measure sample currents. Figure 8 shows the two-step method employed to measure SEY using sample currents, which follows the method outlined by Zameroski *et al.*[50] The primary electron beam current was determined by measuring the sample current with the sample biased to +100 Volts to recapture any electron emissions. The sample current was then re-measured without the sample bias which provided the primary beam current minus the electron emission current. The following formula was then used to calculate the total SEY of the surface (I_{s1} and I_{s2} are defined in Fig. 8):

$$\sigma_{\text{surface}} = \frac{I_{s1} - I_{s2}}{I_{s1}} = \frac{\cancel{I_{\text{primary}}} - (\cancel{I_{\text{primary}}} - I_{\text{emission}})}{I_{\text{primary}}} = \frac{I_{\text{emission}}}{I_{\text{primary}}}. \quad (16)$$

Figure 9 shows the measured SEY curves for the five micro-porous samples as well as a non-porous reference sample for both the electroplated gold and sputtered gold. SEY measurements of the non-porous reference samples provide the empirical data needed for the parameters $\sigma_{\text{non-pore}}$ and $\sigma_{\text{pore-bottom}}$ which are necessary to make SEY predictions using the 2D and 3D models. The difference between the electroplated gold and sputtered gold reference curves shown in Fig. 9 re-emphasizes the importance of maintaining distinct surface SEY parameters ($\sigma_{\text{non-pore}}$ and $\sigma_{\text{pore-bottom}}$) in the analytical models. Evident in the curves shown in Fig. 9 is the effect porosity and aspect ratio have on the total SEY. The slight upward concavity of the curves in Fig. 9, over the energy range 200 to 400 eV, is caused by a thin layer (several nanometers) of the non-native material that becomes adsorbed to the gold surface during exposure to the atmosphere. This unusual bend or "shoulder" in gold SEY curves at low energies has been previously observed and explained by Nistor *et al.* as resulting from "the adventitious surface carbonaceous contamination."[39] Thus, the curve shape in the region where primary electron energy is less than 400 eV more accurately describes the SEY of this thin surface layer of the non-native adsorbed material.

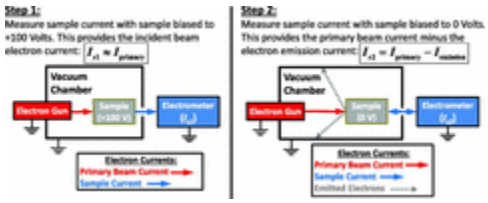

FIG. 8. Illustration of the method used to measure the secondary electron yield.[49]

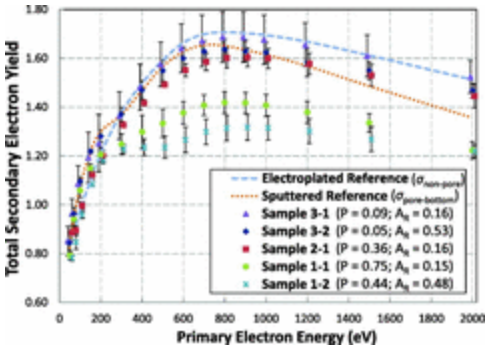

FIG. 9. Measured secondary electron yield curves for microporous gold surfaces[49] (Note: error bars represent a 95% confidence interval assuming that the data follow a Gaussian distribution).

C. Comparison of experimental results to analytical models

Figure 10 shows a side-by-side comparison of the total SEY predictions from the two proposed models as well as the experimentally measured total SEY curves of four micro-porous samples. The curves in Fig. 10 illustrate the improvement in accuracy provided by the 3D model over the curve maxima range (roughly 600 to 1000 eV). The overestimate of SEY at the curve maxima shown in the top two plots of Fig. 10 (Samples 1–1 and 1–2) is directly caused by the pore deformation that occurred during fabrication of these close-packed sample designs. This is because the non-continuous pore sidewalls shown in Fig. 7(a) exposed a greater region of the sputtered gold (i.e., $\sigma_{\text{pore-bottom}}$) which lowered the surface SEY because the sputtered gold has a lower SEY than the electroplated gold (see Fig. 9). Since both the 2D and 3D models are based on perfectly circular and continuous pore sidewalls, their SEY predictions are not reduced by this increase in sputtered gold area and therefore predict larger SEY values. Figure 11 shows the linear relationship, evident in Eq. (1), between porosity and total SEY of the porous surface. Figure 11 also illustrates reasonable agreement between the 3D pore model SEY predictions and the experimentally measured SEY curve maximum of the micro-porous samples. An important observation to make from Fig. 11 is the 3D model prediction that a gold surface with a porosity of 0.5 and an aspect ratio of 2.0 would bring the SEY curve maximum to near unity.

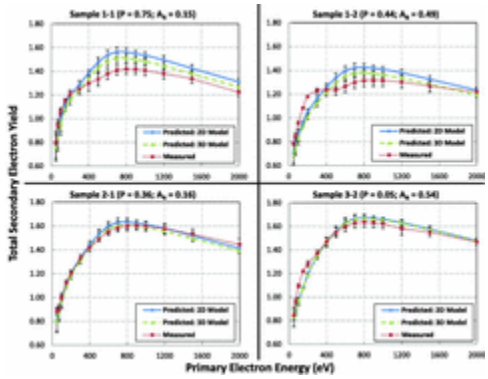

FIG. 10. Comparison of 2D and 3D SEY model predictions with measured SEY curves for micro-porous gold surfaces (Note: error bars represent a 95% confidence interval assuming that the data follow a Gaussian distribution).

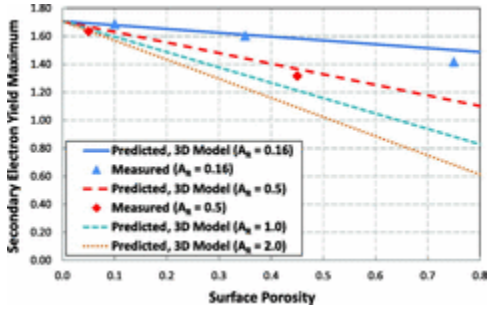

FIG. 11. Plot of 3D micro-porous surface SEY-maxima model predictions and experimentally measured SEY-maxima values for the five micro-porous samples used in this study.

This represents an optimal surface topography for a multipactor-free device using gold surfaces and will be investigated in future experiments.

IV. CONCLUSIONS

Two new semi-empirical models for predicting the SEY of a porous surface were proposed—a simplified model based on a 2D pore structure and a more accurate but complicated model based on a 3D pore structure. These models use SEY measurements of reference samples to more accurately predict the SEY of a micro-porous surface. Model predictions were shown to accurately correspond to SEY measurements of micro-porous gold surfaces of varying porosities and aspect ratios. The SEY model based on the 3D pore structure predicts that a gold surface with pore aspect ratios of 2.0 and a porosity of 0.5 will restrict the SEY curve to unity and below. This provides an engineered surface design to target for a follow-on investigation. Additional investigations should include other materials such as Ag, Cu, and stainless steel as well as if these models are accurate for predicting non-porous surface topographies such as those created from chemical etches and laser treatments.

Engineered surfaces are providing new and effective methods for controlling the SEY of a given material. In multipactor suppression, the primary drawback to using low-SEY coatings is their susceptibility to aging caused by degradation of the coating effectiveness due to chemical changes at the surface. Engineered surfaces overcome this problem by leveraging topographical parameters such as surface feature aspect ratio and distribution density to control the SEY of the material. The tradeoff to using engineered surfaces is their potential impact on RF performance parameters. Thus, it becomes vital to determine optimal surface topographies that reduce SEY to unity or below while minimizing their impact on RF performance. The semi-empirical porous surface SEY models presented in this paper provide new tools to aid research in this field. Although the models were validated with SEY measurements of micro-porous gold surfaces, these models can be applied to other materials and other sizes of pores.

ACKNOWLEDGMENTS

The authors thank Dr. Robert Fitch, Mr. Jason Hickey, Mr. Rich Johnson, and Mr. Adam Fritzsche for providing invaluable support during micro-porous surface fabrication. We also thank Dr. Paul Murray for providing vital perspectives on SEY. Finally, we thank Dr. Christine Schubert Kabban for providing mathematical clarity regarding the random processes involved in this research.

References

1. H. Bruining, J. H. de Boer, and W. G. Burgers, Phys. IV **4**, 267 (1937).
2. H. Bruining, Philips Tech. Rev. **3**, 80 (1938).
3. J. L. H. Jonker, Philips Tech. Rev. **3**, 211 (1938).
4. K. G. McKay, in *Advances in Electronics and Electron Physics*, edited by L. Marton Academic Press Inc., Publishers, New York, 1948), Vol. **I**, pp. 65–120.
5. H. Bruining, *Physics and Applications of Secondary Electron Emission* (McGraw-Hill Book Co., Inc., New York, 1954).
6. A. J. Dekker, Solid State Phys. **6**, 251–311 (1958). https://doi.org/10.1016/S0081-1947(08)60728-6
7. D. H. Preist and R. C. Talcott, IRE Trans. Electron Devices **8**, 243 (1961). https://doi.org/10.1109/T-ED.1961.14797
8. J. R. M. Vaughan, IRE Trans. Electron Devices **8**, 302 (1961). https://doi.org/10.1109/T-ED.1961.14804
9. R. Hayes and D. Preist, in *Research on Microwave Window Multipactor and Its Inhibition* (U.S. Army Electronics Laboratories, Fort Monmouth, New Jersey, 1965).
10. Hughes Aircraft Company, *The Study of Multipactor Breakdown in Space Electronic Systems* (Hughes Aircraft Company, Culver City, CA, 1966).
11. A. J. Hatch, Nucl. Instrum. Methods **41**, 261 (1966). https://doi.org/10.1016/0029-554X(66)90010-3
12. D. J. Lewis and D. K. McCarty, Proc. IEEE **54**, 713 (1966). https://doi.org/10.1109/PROC.1966.4832
13. J. E. Stern and K. R. Mercy, in *Proceedings of the Second Workshop on Voltage Breakdown in Electronic Equipment at Low Air Pressures*, edited by E. R. Bunker (1969), pp. 3–8.
14. G. August and J. B. Chown, in *Proceedings of the Second Workshop on Voltage Breakdown in Electronic Equipment at Low Air Pressures*, edited by J. E. R. Bunker (Jet Propulsion Laboratory, Pasadena, CA, 1969), pp. 193–201.
15. H. Jahrreiss, Thin Solid Films **12**, 187 (1972). https://doi.org/10.1016/0040-6090(72)90413-0
16. C. M. Lyneis, H. A. Schwettman, and J. P. Turneaure, Appl. Phys. Lett. **31**, 541 (1977). https://doi.org/10.1063/1.89770
17. W. J. Gallagher, IEEE Trans. Nucl. Sci. **26**, 4280 (1979). https://doi.org/10.1109/TNS.1979.4330768
18. C. M. Lyneis, J. Sayag, H. A. Schwettman, and J. P. Turneaure, IEEE Trans. Nucl. Sci. **26**, 3755 (1979). https://doi.org/10.1109/TNS.1979.4330601
19. P. J. Tallerico, IEEE Trans. Nucl. Sci. **30**, 3420 (1983). https://doi.org/10.1109/TNS.1983.4336677
20. R. Boni, V. Chimenti, P. Fernandes, R. Parodi, B. Spataro, and F. Tazzioli, IEEE Trans. Nucl. Sci. **32**, 2815 (1985). https://doi.org/10.1109/TNS.1985.4334191
21. S. R. Farrell and W. J. Gallagher, IEEE Trans. Nucl. Sci. **32**, 2900 (1985). https://doi.org/10.1109/TNS.1985.4334220
22. A. R. Nyaiesh, E. L. Garwin, F. K. King, and R. E. Kirby, *Properties of Thin Anti-Multipactor Coatings for Klystron Windows* (Stanford Linear Accelerator Center, Stanford, CA, 1985).
23. W. Weingarten, IEEE Trans. Electr. Insul. **24**, 1005 (1989). https://doi.org/10.1109/14.46328

[24] W. R. Fowkes, R. S. Callin, and A. E. Vlieks, in *Linear Accelerator Conferences* (Stanford Linear Accelerator Center, Stanford, California, 1992).
[25] F. Le Pimpec, R. E. Kirby, F. King, and M. Pivi, J. Vac. Sci. Technol., A **23**, 1610 (2005). https://doi.org/10.1116/1.2049306
[26] M. Kuchnir and E. Hahn, *Coating Power RF Components with TiN* (Fermi National Accelerator Laboratory, Bativa, IL, 1995).
[27] D. Proch, D. Einfeld, R. Onken, and N. Steinhauser, in *Proceedings of the 1995 Particle Accelerator Conferences* (1995), pp. 1776–1778.
[28] J. Tuckmantel, C. Benvenuti, D. Bloess, D. Boussard, G. Geschonke, E. Haebel, N. Hilleret, S. Juras, H. P. Kindermann, J. Uythoven, C. Wyss, and M. Stirbet, in *Proceedings of the 1995 Particle Accelerator Conferences* (IEEE, Dallas, TX, 1995), pp. 1642–1644.
[29] N. Díaz, S. Castañeda, J. M. Ripalda, I. Montero, L. Galán, S. Feltham, D. Raboso, and F. Rueda, in *6th Spacecraft Charging Technology Conference* (2000), pp. 205–209.
[30] J. Lorkiewicz, A. Brinkmann, B. Dwersteg, D. Kostin, W.-D. Moeller, and M. Layalan, in *Proceedings of the 10th Workshop on RF Superconductivity: SRF 2001* (High Energy Accelerator Research Organization, 2003), pp. 448–452.
[31] S. Michizono, Y. Saito, Suharyanto, Y. Yamano, and S. Kobayashi, Appl. Surf. Sci. **235**, 227 (2004). https://doi.org/10.1016/j.apsusc.2004.05.131
[32] G. G. Fuentes, R. J. Rodríguez, M. García, L. Galán, I. Montero, and J. L. de Segovia, Appl. Surf. Sci. **253**, 7627 (2007). https://doi.org/10.1016/j.apsusc.2007.03.065
[33] I. Montero, S. H. Mohamed, M. García, L. Galán, and D. Raboso, J. Appl. Phys. **101**, 113306 (2007). https://doi.org/10.1063/1.2736861
[34] A. Ruiz, E. Román, P. Lozano, M. García, L. Galán, I. Montero, and D. Raboso, Vacuum **81**, 1493 (2007). https://doi.org/10.1016/j.vacuum.2007.04.007
[35] Suharyanto, S. Michizono, Y. Saito, Y. Yamano, and S. Kobayashi, Vacuum **81**, 799 (2007). https://doi.org/10.1016/j.vacuum.2005.11.062
[36] N. Balcon, D. Payan, M. Belhaj, T. Tondu, and V. Inguimbert, IEEE Trans. Plasma Sci. **40**, 282 (2012). https://doi.org/10.1109/TPS.2011.2172636
[37] M. Ye, Y. N. He, S. G. Hu, J. Yang, R. Wang, T. C. Hu, W. B. Peng, and W. Z. Cui, J. Appl. Phys. **114**, 104905 (2013). https://doi.org/10.1063/1.4821138
[38] M. Ye, Y. N. He, S. G. Hu, R. Wang, T. C. Hu, J. Yang, and W. Z. Cui, J. Appl. Phys. **113**, 074904 (2013). https://doi.org/10.1063/1.4792514
[39] V. Nistor, L. A. González, L. Aguilera, I. Montero, L. Galán, U. Wochner, and D. Raboso, Appl. Surf. Sci. **315**, 445–453 (2014). https://doi.org/10.1016/j.apsusc.2014.05.049
[40] R. Valizadeh, O. B. Malyshev, S. Wang, S. A. Zolotovskaya, W. A. Gillespie, and A. Abdolvand, Appl. Phys. Lett. **105**, 231605 (2014). https://doi.org/10.1063/1.4902993
[41] L. Cai, J. Wang, G. Cheng, X. Zhu, and H. Xia, J. Appl. Phys. **117**, 53302 (2015). https://doi.org/10.1063/1.4907683
[42] R. Valizadeh, O. B. Malyshev, S. Wang, T. Sian, M. D. Cropper, and N. Sykes, Appl. Surf. Sci. **404**, 370 (2017). https://doi.org/10.1016/j.apsusc.2017.02.013
[43] S. Riyopoulos, D. Chernin, and D. Dialetis, Phys. Plasmas **2**, 3194 (1995). https://doi.org/10.1063/1.871151
[44] Y. Li, W.-Z. Cui, N. Zhang, X.-B. Wang, H.-G. Wang, Y.-D. Li, and J.-F. Zhang, Chin. Phys. B **23**, 48402 (2014). https://doi.org/10.1088/1674-1056/23/4/048402

[45.] M. Buyanova, V. E. Semenov, D. Anderson, M. Lisak, and J. Puech, Phys. Plasmas **17**, 043504 (2010). https://doi.org/10.1063/1.3374430
[46.] O. Hachenberg and W. Brauer, in *Advances in Electronics and Electron Physics* (Academic Press, New York, 1959), Vol. XI, pp. 413–499.
[47.] D. C. Joy, *A Database Electron-Solid Interactions* (2008), available at http://studylib.net/doc/5878300/a-database-of.
[48.] J. M. Sattler, R. A. J. Coutu, R. A. Lake, and T. Laurvick, in *IEEE National Aerospace and Electronics Conference and Ohio Innovation Summit* (Institute of Electrical and Electronics Engineers (IEEE), Dayton, 2016), pp. 296–302.
[49.] J. M. Sattler, R. A. J. Coutu, R. A. Lake, and T. Laurvick, in *9th International Workshop on Multipactor, Corona Passive Intermodulation* (Noordwijk, 2017).
[50.] N. D. Zameroski, P. Kumar, C. Watts, T. Svimonishvili, M. Gilmore, E. Schamiloglu, and J. A. Gaudet, IEEE Trans. Plasma Sci. **34**, 642 (2006). https://doi.org/10.1109/TPS.2006.875778